
Chapter 3

*Extraordinary magnetic properties of double
perovskite $\text{Eu}_2\text{CoMnO}_6$ wide band gap Semiconductor*

3.1 Introduction

By means of the J. C. Maxwell's equations, interconnecting the dynamics of electric fields, magnetic fields, and electric charges, it was inferred that the magnetic interactions and motion of electric charges are not independent but intrinsically coupled to each other showing unification of magnetism and electricity [126]. The materials with such extraordinary, multi-functional properties are gained much more interest due to their attractive, well-to-do physics and panorama for technological device applications [127–129]. In the last few decades, people are trying to search for such new multi-functional materials for next-generation spintronic devices [3,130–137]. In this regard, the rare earth double perovskite (DP) oxides, $A_2BB'O_6$ (A= rare earth ions or alkaline ions; B/B' = transition metal ions) with rock salt ordered structure are of great importance for their multi-functional properties. DPs are ferromagnetic insulators driven by the electron correlations possessing high magnetic transition temperatures (close to room temperature) [4,5,63,138–142]. In addition, they display room-temperature magneto-capacitance, giant magneto-resistance, colossal magneto-dielectric, ferro-electricity, spin-glass transition, exchange bias, spin reorientation, local atomic disorder and formation of anti-phase domains, Griffiths phase, the existence of spin-phonon coupling etc [4,5,63,138–142]. Furthermore, the existence of multi-ferroicity in DPs (e.g., in La_2NiMnO_6 , Y_2CoMnO_6) have been theoretically predicted using first-principle density functional calculations [143–147]. Nevertheless, these properties can be tuned by changing valencies of the transition metals, size of cations and environmental chemical pressure. Moreover, magnetic properties are strongly influenced by the presence of antisite disorder in the system due to the change of B-O-B' exchange interaction path [34,148–151].

Moreover, DPs having “A” site nonmagnetic ions such as La, Y, Lu, Eu [5,120,122,152,153] has recently drawn extensive attention due to their distinctive magnetic behavior. As magnetic and other physical properties of DPs are mainly determined by the valence state of the transition-metal cations B and B' by means of their exchange interaction with each other and with the rare earth metal ions, the interactions between rare-earth ions (A being nonmagnetic) and transition metal ions can be neglected. The most intriguing feature observed in Y_2CoMnO_6 [5,120,153] and $\text{Lu}_2\text{CoMnO}_6$ [153] is the meta-magnetic transition (MMT) in the isothermal magnetization curve. Generally, MMT is observed in certain phase-separated manganites and in a few inter-metallics like Gd_5Ge_4 [130–133]. Materials with the coexistence of MMT and giant magneto-caloric effect has great importance in solid-state cooling technology like highly efficient magnetically cooled refrigerator [134–137]. The step positions change with temperature and sweep rate of the external magnetic field and also the steps are more prominent at a lower temperature.

In fact, $\text{Eu}_2\text{CoMnO}_6$ with nonmagnetic Eu^{3+} is the much less studied system [152]. The end members of this family are EuMnO_3 and EuCoO_3 . In EuMnO_3 , an incommensurate antiferromagnetic structure is observed at 52 K and an *A*-type antiferromagnetic ordering is found at 48 K [154]. On the other hand, EuCoO_3 is a nonmagnetic compound even down to low temperature, the energy splitting in Co^{3+} ions between low spin ($S=0$) and the intermediate spin states ($S=1$) is ~ 2200 K [155]. Starting from EuMnO_3 , the ferrimagnetic spin ordering temperature increases with Co doping to 120 K and decreases for higher Co concentrations [156]. Therefore, exploring the properties of $\text{Eu}_2\text{CoMnO}_6$ may unravel new interesting magnetic states. In this chapter, along with MMT we have shown the existence of Griffiths like phase, strong spin-glass-like behavior, and Hopkinson like effect in $\text{Eu}_2\text{CoMnO}_6$.

3.2 Experimental

Polycrystalline DP $\text{Eu}_2\text{CoMnO}_6$ (ECMO) was synthesized by the conventional solid-state reaction method. Stoichiometric mixture of high-purity Eu_2O_3 , CoO and Mn_2O_3 were ground and calcined at 1000°C , 1100°C and 1250°C for 24 hours each with intermediate grindings. The final sintering was made at 1300°C for 48h. Powder X-ray diffraction (XRD) was performed by using RigakuMiniflex II X-ray diffractometer ($\text{Cu-K}\alpha$) to check the phase purity of the samples and was refined by Rietveld method using FULLPROF suite software. The magnetic measurements were performed by a quantum design magnetic property measurement system (Quantum design-MPMS) superconducting quantum interference device (SQUID) magnetometer. The XPS (X-ray photoemission spectroscopy) study was carried out using an Omicron Multi-probe Surface Science System, equipped with a monochromatic source (XM 1000) and a hemispherical electron energy analyzer (EA 125). While performing the XPS measurement the average base pressure was kept about 6.1×10^{-10} torr with a power of ≥ 280 W. The total energy resolution was estimated around 0.25 eV for the monochromatic Al K_α line at 15 kV. The pass energy for the wide-surface scan spectrum and the core level spectrums was maintained at 50 eV and 30 eV respectively. The non-monochromatic He I line was used for ultraviolet photoemission spectroscopy (UPS) measurements with the average base pressure of 3.1×10^{-8} torr. The UV–Visible absorption spectra were measured by the Lambda–35 UV–Vis spectrophotometer from Perkin Elmer.

3.3 Results and discussions

3.3.1 X-ray diffraction study

The X-ray diffraction of ECMO taken at room temperature with Rietveld refinement is shown in Fig. 1. The crystal refinement fitting match well to an orthorhombic crystal structure with a space group $Pnma$ as well as it can also be fitted with an ordered monoclinic structure with space group $P21/n$ with comparable unit cell volume. However, as according to the crystallography, the orthorhombic crystal structure has higher symmetry than the monoclinic

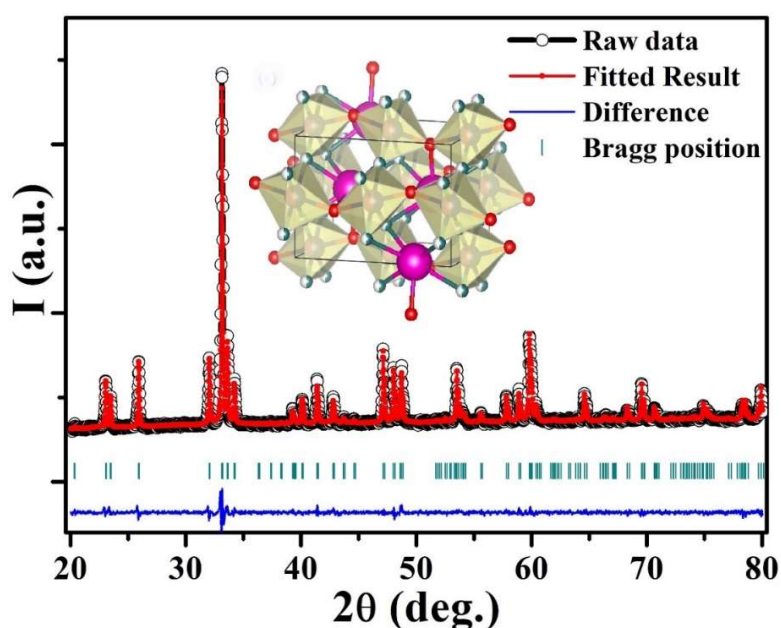


Figure 3.1: X-Ray diffraction pattern with Rietveld refinement and the structure of ECMO indicating the tilted chains of $(Co/Mn)O_6$ octahedra.

the actual space group should be $Pnma$. Vasiliev et. al., also reported the orthorhombic crystal structure in $EuCo_{0.5}Mn_{0.5}O_3$ [152]. Further any other impurity phases were not observed suggesting the existence of a single phase. This disordered orthorhombic phase entails the random distribution at B-sites of Co/Mn ions. The inset of Fig. 3.1 represents the structure of ECMO obtained from VESTA, showing the three-dimensional array of $(Co/Mn)O_6$ octahedral. The crystallographic information, from the refinement data are summarized in Table 4.1.

3.3.2 X-ray photoemission spectroscopy study

In order to explore the magnetic as well as electrical properties, we have carried out X-ray photoemission spectroscopy (XPS) measurement, as shown in Fig. 3.2(a-f). The wide-surface-scan XPS spectra of the ECMO sample is shown in Fig. 3.2(a) and all peaks are allocated according to the National Institute of Standards and Technology (NIST) database. The existence of Eu, Co, Mn and O at the surface is observed from the spectrum. Additionally, only presence of the carbon (C) impurity at 284.7 eV was detected in the spectrum, as it always gets absorbed from the air at the surface of the sample. The core-level Eu3d XPS spectrum region of ECMO is shown in Fig. 3.2(b) and peaks were fitted using XPSPEAK41 software. As a result of strong spin-orbit coupling, the binding energies of Eu3d core-level have two intense peaks: Eu3d_{3/2} (1163.8 eV) and Eu3d_{5/2} (1133.9 eV) separated by 29.9 eV. Fitting of Eu3d peaks confirms the existence of Eu³⁺ state (~94.3%) due to the 3d4f⁶ configuration. Moreover, the Eu3d_{3/2} core level shows a satellite (S) peak around 1156 eV which corresponds to the Eu²⁺ state (~5.7%) which is attributable to the 3d4f⁷ final state configuration [157]. Additionally, a low intense peak was observed above the Eu3d_{3/2} peak manifesting as “M_Eu³⁺” around 1142.5 eV, which is apparently related to the multiplet effect due to the coupling between the open-shell and a core electron vacancy and is reported as a satellite peak [158]. Calculation of area under the corresponding peak fitted curves give the relative concentration of Eu³⁺ states about 94.3% and that of Eu²⁺ states about 5.7% respectively on the surface. Reason behind the presence of Eu²⁺ states might be due to the oxygen vacancies or due to formation of some OH⁻ ions which is shown in the inset of Fig. 3.2(e) as O²⁻ loss in O1s XPS spectra.

The core-level Co2p peak fitted XPS spectrum of ECMO is shown in Fig. 3.2(c). Due to spin-orbit coupling, it has two narrow intense peaks centered around 779.7 eV ($2p_{3/2}$) and around 795.4 eV ($2p_{1/2}$) corresponding to Co^{3+} states [159,160]. With the deconvolution, relatively broad intense peaks of Co^{2+} states centered around 781.1 eV corresponding to $2p_{3/2}$ and around 797.1 eV corresponding to $2p_{1/2}$ are observed. Additionally, two peaks around 786.2 eV and 802.5 eV were observed which correspond to shake-up satellite peak and they are very sensitive to valence states of cation, the coordination number of ligands, etc. The relative concentration of Co^{2+} states was calculated to be about 59% and that of Co^{3+} states about 41% respectively. The core-level Co3s peak fitted XPS spectrum shows an intense peak around 100.6 eV (Fig. 3.2(e)) and a buried peak about 106.2 eV which arises due to the exchange interactions among the core hole and the open 3d shell [161,162].

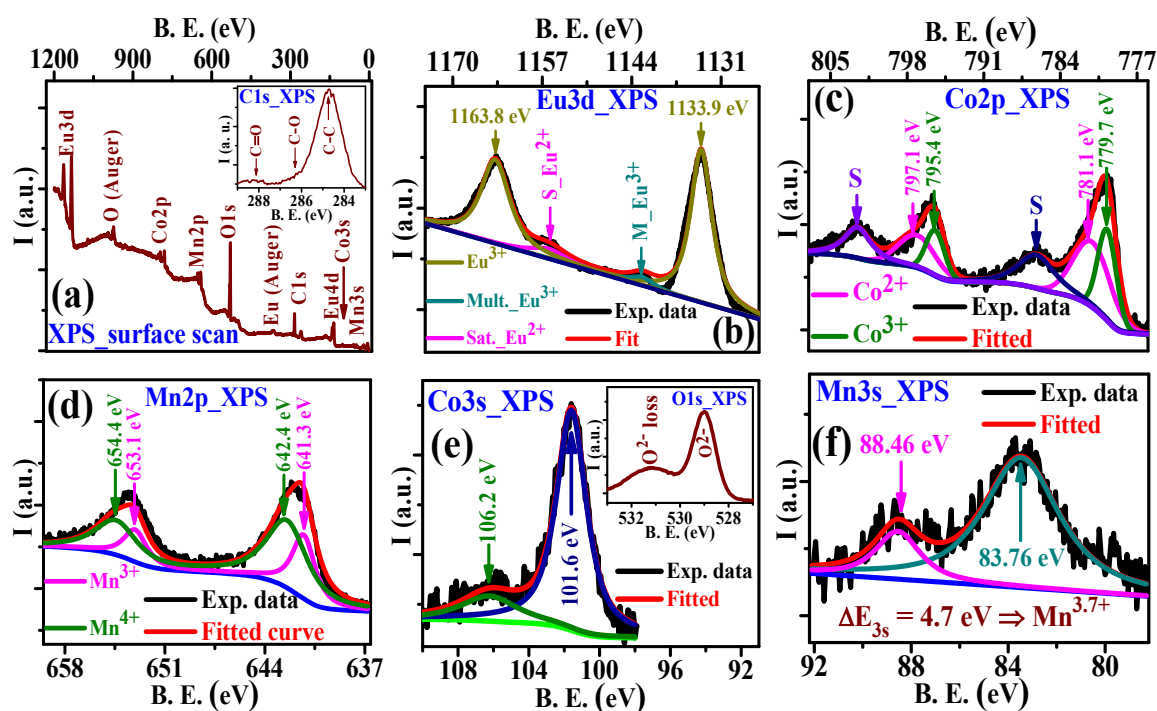


Figure 3.2: (a-f) Wide-range-surface scan & core-level X-ray photoemission spectroscopy (XPS) of different constituent elements of ECMO.

Similarly, the core-level Mn2p spin-orbit coupling spectra show two peaks corresponding to Mn2p_{3/2} and Mn2p_{1/2} respectively with a doublet separation of ~12 eV (Fig. 3.2(d)). XPS peak fitting of the Mn2p region confirm two mixed valence states of Mn, i.e., Mn³⁺ (~34%) and Mn⁴⁺ (~66%) as Mn2p_{3/2} are deconvoluted into two peaks centered around 641.3 eV (Mn³⁺) and 642.4 eV (Mn⁴⁺) while the Mn2p_{1/2} peaks are deconvoluted around 653.3 eV (Mn³⁺) and 654.4 eV (Mn⁴⁺) [163]. Further, these Mn valence states were verified more quantitatively by taking Mn3s XPS spectra. Fig. 3.2(f) shows peak fitted XPS spectrum of Mn3s core-level. Two exchange split peaks centered around 83.76 eV and 88.46 eV were observed (with $\Delta E_{3s} \sim 4.7$ eV). ΔE_{3s} is directly related with Mn valence state (V_{Mn}) by the relation [164], $V_{Mn} = 9.67 - 1.27 \times \Delta E_{3s}$ (in eV). The obtained Mn valence states from the above relation is about 3.7+, supporting the mixed valency is consistent with the Mn2p XPS spectra.

3.3.3 UPS and UV-visible spectroscopy study

Fig. 3.3(a) shows the UPS valence band spectra of ECMO. It contains the basic ground state electronic structure information. The UPS spectrum is more sensitive for lighter atoms due to lower photon energy. Thus, the dominant peak near 6 to 9 eV in the UPS valence band spectra is assigned to emission from O2p states [163,164]. The buried spectrum below 3 eV corresponds to different Mn3d states where the characteristics around 2.4 eV corresponds to Mn3d(*t_{2g}*), while around 1 eV is attributed to Mn3d(*e_g*) states. Further high-resolution UPS spectra were taken (shown in the inset of Fig. 3.3(a)) near Fermi-level (E_f) to see ground state electronic structure more accurately. There are no finite electronic states present at E_f suggesting the semi-conducting/insulating nature of ECMO at room temperature. This is also

consistent with the high electrical resistivity value at room temperature ($\sim 10^5 \Omega \text{ cm}$). Further analysis shows the existence of two valence band edges, respectively, at 1 eV and 2.4 eV.

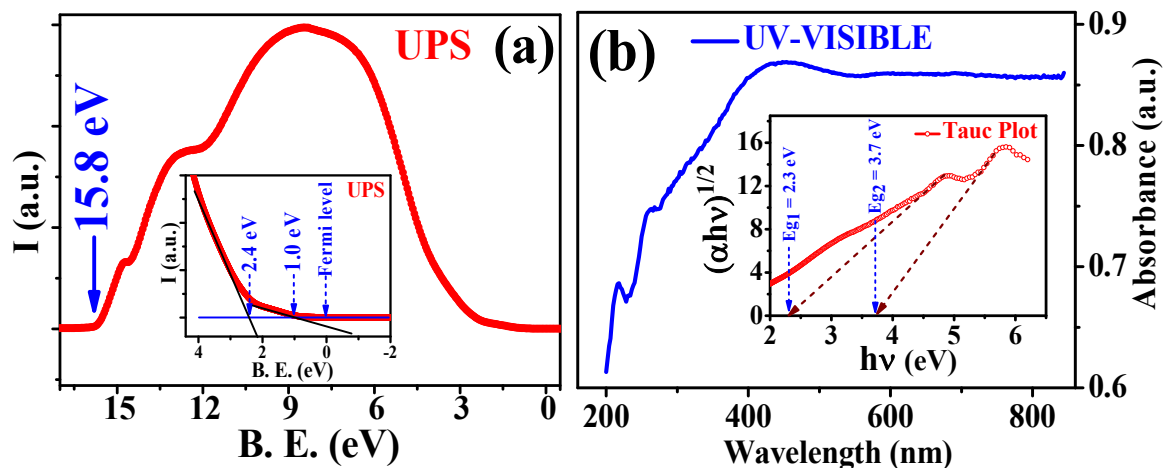


Figure 3.3: (a) The ultraviolet photoemission spectra along with insets showing the high Fermi level. (b) The UV-Visible absorption spectrum along with inset showing Tauc plot of ECMO.

Therefore, it is worthwhile to mention that the valence band maximum exists at 1eV. From the UPS spectra lower cut-off energy is found around 15.8 eV while measurements were performed using ~ 21.2 eV photon energy line. Thus, the electronic work function of ECMO is estimated to be around 5.4 eV. Moreover, the energy band gap and change in electron distribution due to charge transfer from ligands to the metal play an important role in optical properties. Ultraviolet-visible (UV-Visible) spectroscopy is an important tool to determine the energy band-gap. The UV-Visible absorption spectrum of the ECMO is shown in Fig. 3.3(b). This absorption spectrum shows that ECMO is capable to absorb UV region photon as well as it has large absorbance capacity in the visible region too. The inset of Fig. 3.3(b) shows the Tauc plot, demonstrating direct band-gap material. The energy band gap (E_g) related with the ECMO was determined from the relation, $\alpha h\nu = A(h\nu - E_g)^n$ [165,166], where, ν is the

frequency of the photon, h is the Planck constant, A is constant, and $n = 1/2$ for an allowed direct electronic transition. Tauc plot shows that ECMO has a double band gap, with the energy band gap of $E_{g1} = 2.3$ eV and that of $E_{g2} = 3.7$ eV [167,168]. Thus, ECMO can be used as a wide-band-gap semiconductor. The observed E_{g2} might be due to the transition within ECMO. On the other hand, E_{g1} might be the result of the induced defect state due to oxygen deficiency as has been discussed above.

3.3.4 Magnetic study

Temperature variation of zero field cooling and field cooling (ZFC and FC) magnetization (M) of ECMO at two different applied fields are shown in Fig. 3.4(a). The large bifurcation between the ZFC and FC curves is observed, and the magnitude of bifurcation increases as applied field increased from 100 Oe to 20 kOe and then it gets decreased at 30 kOe. The bifurcation might be the indication of a typical spin-glass state. However, it is not a sufficient feature of typical spin-glass which may also arise from the domain structure of a ferromagnetic material or due to magnetic anisotropy. In order to clarify this issue, we have performed ac susceptibility measurements (discussed later).

From Fig. 3.4(a) it is clear that ZFC magnetization of the ECMO has a small narrow maximum with a cusp at a temperature $T_a \sim 123.2$ K at 100 Oe and at ~ 120.3 K at 1kOe field. Further, these maximally get broaden at the higher magnetic field (10 kOe, 20kOe, 30 kOe) and exhibits a plateau-like anomaly along with a shift in cusp temperature (T_a) toward slower temperature as magnetic field increases (H), and $T_a \propto H$ [shown in the inset of Fig. 3.4(b)]. This might be due to a competition between the local anisotropy and the effect of the external magnetic field, and the cusp at temperature T_a is the temperature where the two energies are

almost of equal magnitude i.e., anisotropy energy and the energy caused by the external field. The bell-like behavior around T_a correlates with the coexistence of low-temperature E^* -type anti-ferromagnetism (AFM) and ferromagnetism (FM). Through Curie-Weiss (CW) analysis of magnetization using the CW relation, $\chi = C/(T - T_{CW})$ and $C = N\mu_{eff}^2/3K_B$, we found an effective paramagnetic moment value of $\mu_{eff} = 7.7\mu_B$, and Curie-Weiss temperature, T_{CW} was found to be around 98 K, implying a dominant ferromagnetic phase due to $Co^{2+}-O^{2-}-Mn^{4+}$ exchange interactions. There might exist anti-ferromagnetic phase due to $Co^{2+}-O^{2-}-Co^{2+}$ and $Mn^{4+}-O^{2-}-Mn^{4+}$ interactions which can be explained by the Goodenough-Kanamori rules [34,148]. Further $T_{CW} < T_C$, which is insignificant if we consider it due to some quantum fluctuation. This might be due to competition between FM and AFM exchange interactions. The magnetization data for $T > 200K$ ($\sim 2T_{CW}$) was used for the CW analysis. It is worthwhile to mention that magnetic ordering of Eu^{2+} (due to oxygen deficiency) is 19 K [169], but no signature of ordering is observed in $M(T)$ curve. The reason behind this might be the magnetic ordering of Eu^{2+} is overwhelmed by the exchange interactions due to Co and Mn.

A clear low-temperature compensation point followed by negative magnetization is observed in the zero field-cooled curves. This may be due to several reasons like formation of canted ferromagnetic domains or anti-parallel spins and clusters that are separated by anti-phase boundary, residual trapped magnetic field in solenoids of the superconducting magnetometer, presence of diamagnetic Co^{3+} ions, as well as dominating anti-ferromagnetic clusters of transition metal ion pairs and anti-ferromagnetically coupled rare earth magnetic moments at low temperature. There is a sudden increase in magnetization below the temperature 124.5 K (which is the temperature T_C , where the derivative of MZFC-T curve exhibits a maximum as shown in Fig. 3.4(b)). This is a sign of magnetic transition at

temperature T_C , and it was found that transition temperature increases with the magnetic field as $T_C \propto H^{2/3}$ (shown in the inset of Fig. 3.4(b)). Between temperature ranges, 124.5 to 200 K,

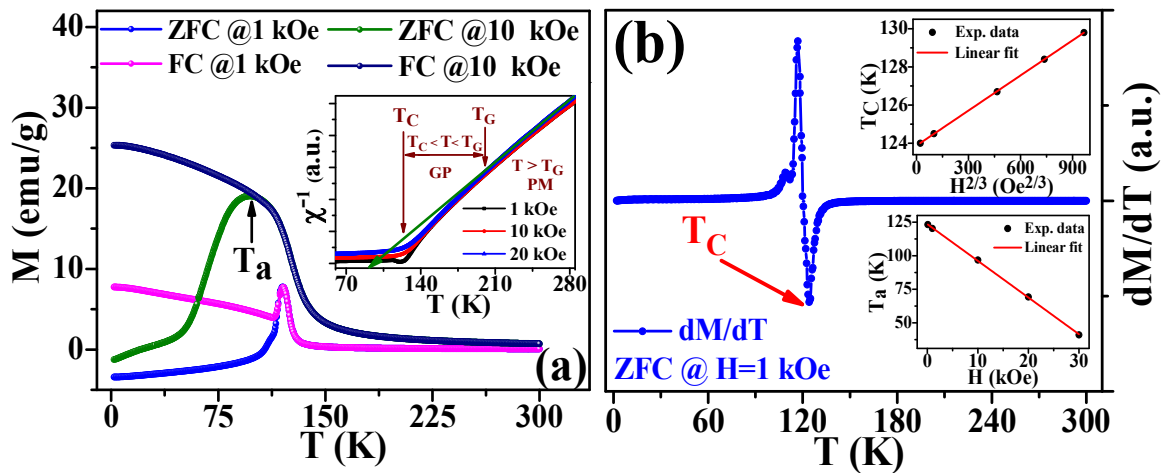


Figure 3.4: (a) The thermal variation of magnetization curves at two different applied ZFC and FC conditions with inset showing inverse DC susceptibility as a function of temperature. (b) The derivative of MZFC– T curve with inset showing variation of T_C & T_a with H .

nature of magnetic states was understood by inverse DC susceptibility (χ^{-1}) vs. temperature (T) curve at different applied fields. It has a slight down-turn deviation from linear variation (CW behavior) below 200 K (T_G) and above magnetic ordering temperature ~ 125 K. Therefore, there is nucleation of small but finite sized correlated regions and clusters with short-range magnetic ordering in paramagnetic matrix which is the signature behavior of Griffiths like phase [101,122].

The isothermal magnetizations vs. field curves of ECMO at different temperatures are shown in Fig. 3.5. The magnetization isotherms at 2 K displays sharp steps and at higher temperature sharpness of these steps disappear. These jumps are seen only while increasing

field i.e., for 0T to 5T and are absent in decreasing field i.e., for 5T to 0T due to slow spin relaxation and re-appear in subsequent negative field direction i.e., for 0T to -5T followed by

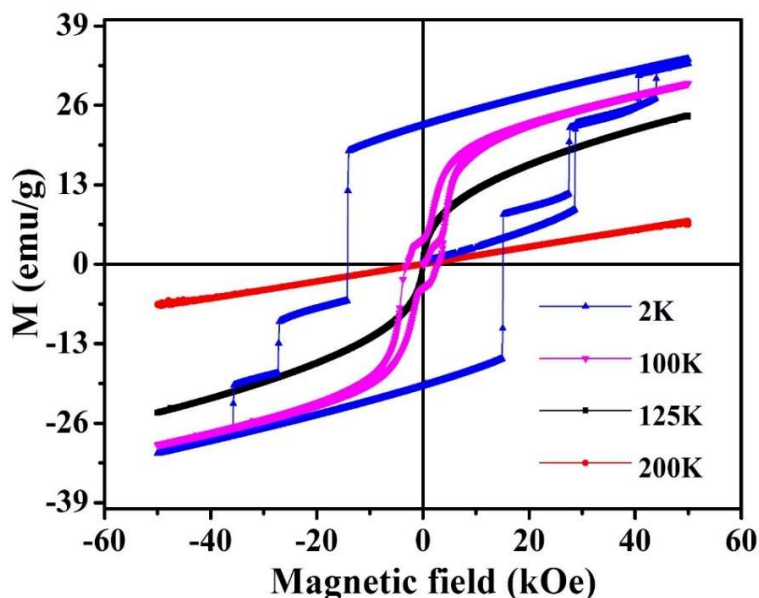


Figure 3.5: The isothermal magnetizations vs. magnetic field of ECMO at 2K, 100K, 125 K, 200 K respectively.

a large remanence and coercivity. In some multiferroic materials e.g., in $\text{Ca}_3\text{CoMnO}_6$ [141,170,171] field-induced sharp jump is assumed to be due to spin flop transition from E^* -type magnetic ordering ($\uparrow \uparrow \downarrow \downarrow$) to the ($\uparrow \uparrow \uparrow \downarrow$) Mn^{4+} (high spin state, $S = 3/2$) at first critical field H_{C1} and to ($\uparrow \uparrow \uparrow \uparrow$) with Co^{2+} (low spin state, $S = 1/2$) at second critical field H_{C2} . Similarly, the origin of metamagnetic transition (MMT) in Y_2CoMnO_6 has been tried to explain with the field-induced spin reorientation of Co and Mn ions [33, 55]. But the observed discontinuity in Y_2CoMnO_6 was not consistent with the spin flop of Co^{2+} (high spin $S = 3/2$) to the ($\uparrow \uparrow \uparrow \uparrow$) magnetic structure at second jump [59]. A similar problem can be seen in ECMO too. Other than this, these discontinuous jumps in magnetization might be due to spin

flopping and magnetic-field-induced lattice distortion (martensitic-like transition), giving rise to transition between the AFM and FM states (i.e., MMT), obtained for certain critical values of the external magnetic field. The reason behind this martensitic like-transition is strong lattice distortion by an external magnetic field via magneto-elastic coupling which gives rise to a crystallographically distorted FM phase. Due to this distortion, an elastic strain develops at the FM/AFM anti-phase interface. The FM phase advances when an external magnetic field is applied, but magneto-striction energy (the energy which opposes the interfacial/martensitic strain) go up against this to stop the expansion of the FM phase.

Besides above, it is possible that while cooling the sample in zero field mode, at a lower temperature, the AFM ordering will lead along with little FM clusters separated by an antiferromagnetic, antiphase boundary (APB). The main reason behind the pinning of Co-O-Mn ordered FM domains in antiparallel is strong AFM Co-O-Co or Mn-O-Mn interactions across the APB that orient neighboring FM domains in antiparallel [59,108]. For the case, when we increase the magnetic field during the isothermal magnetization process, the FM domain will try to grow, however, due to opposing forces, there is a small change in the magnetization. At a critical field H_{C1} , the energy of the external field is so high that it can overcome the magneto-striction energy related to the FM/AFM anti-phase boundary and some of the spins from AFM domain flop along the field direction, giving rise to a sudden increase in magnetization. This process leads to an increase in elastic energy and decrease in the magneto-static energy, a balance which can show the way to the system to go in another metastable state. As we further increase the external magnetic field it will reach to another critical value H_{C2} , so that it again flops few spins and cause the second step in isothermal

magnetization. Thus, overall transitions proceed by successive jumps between one meta-stable state to another.

For more information regarding spin-structure, we have carried out ac susceptibility measurement. Fig. 3.6(a, b) shows the temperature dependence of in-phase (χ') and out of phase component (χ'') of AC susceptibility at different frequencies and constant AC field of 3 Oe without any DC bias. We observed unusual sharp peaks in ac susceptibility near $T_C \sim 124$ K which might be due to magnetic ordering or spin glass transition. The peaks do not shift with the frequency indicating the absence of a typical spin glass behavior. As the peaks are sharp and narrow, the spins of all ions of ECMO relax with almost equal relaxation time. Further, the out of phase component of ac susceptibility indicates that smaller peaks show short-range ordering. More interestingly, prior to short-range ordering, there is a slight deviation in ac susceptibility from its zero value which is in favor of signature behavior of a typical Griffiths like phase.

Fig. 3.6(c, d) shows the temperature dependence of in-phase (χ') and out of phase component (χ'') of ac susceptibility with different DC bias at a constant frequency of 500 Hz and constant AC field of 3 Oe. Here, again similar unusual sharp peak in AC susceptibility was observed near T_C , more interestingly this peak is suppressed, broadened and split into two maxima with increasing DC bias. The peak which is at the higher temperature, T_{high} shifts towards the higher temperature side on increasing DC bias. It is to be noted that there is a similar variation in T_C obtained by the M–T curve which shifts towards the high-temperature side as we go for high field ZFC/FC curves. This is consistent with the shift of the T_{high} with the external dc magnetic field, which is recognized to be the presence of critical fluctuations associated with a continuous transition to a ferromagnetic state. While the peak which is at a

lower temperature, T_{low} shifts towards the lower temperature side on increasing DC bias. In phase component of AC susceptibility is expected to be constant below the PM to FM transition temperature. However, in a few magnetic oxide systems in which the finite size of FM and AFM clusters coexist, $\chi'(T)$ decreases below the transition. This phenomenon is known as

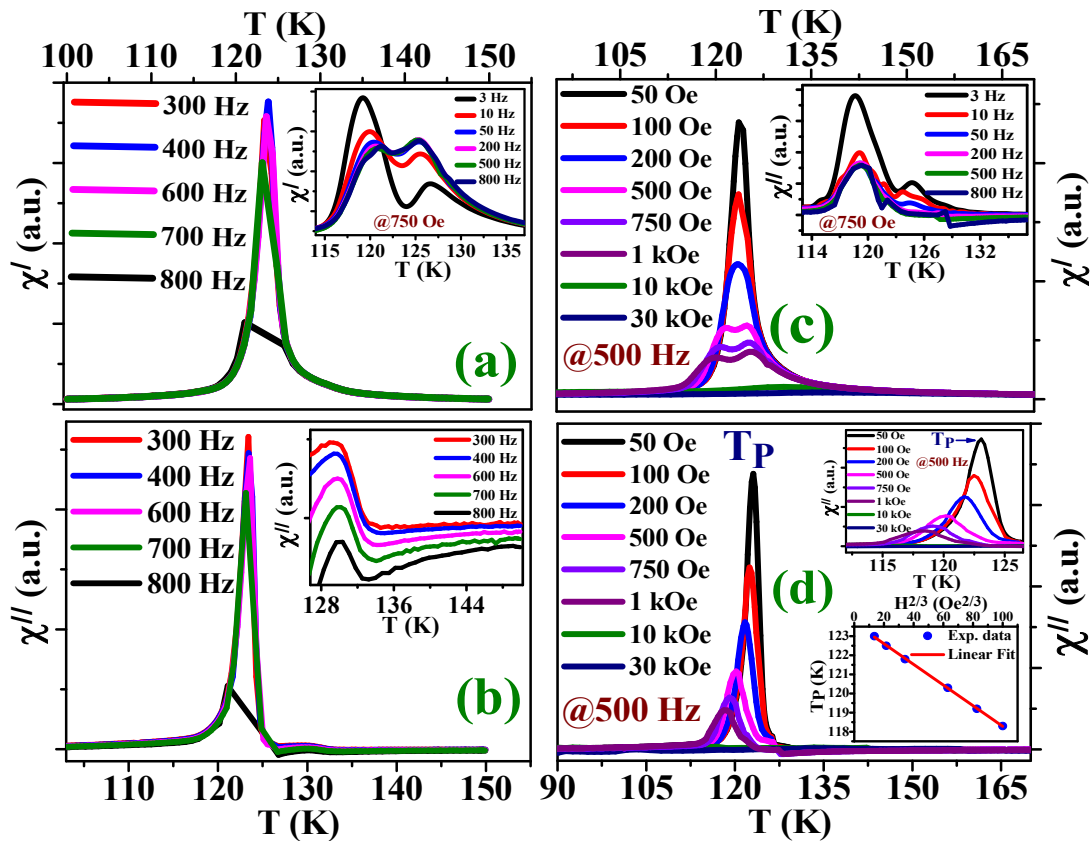


Figure 3.6: The thermal variation of ac susceptibility χ' and χ'' (a & b) at different frequencies without DC, (c & d) at constant frequency and with different DC bias along with inset showing AT line. The inset of (a) & (c) is showing the ac susceptibility χ' and χ'' at different frequencies with constant DC bias, $H = 750$ Oe

Hopkinson effect which is related to magnetic anisotropy/inhomogeneity. Change in magnetic anisotropy arises on decreasing temperature due to continuous change in size and shape of FM clusters below the transition [107,172]. Hopkinson effect is attributed to the competing spin-spin correlations and large anisotropy field compared to the measurement field which can be

explained by the relation, $\chi'(T) \propto M_S^2(T)/K(T)$ [172], where, $M_S(T)$ is the spontaneous magnetization and $K(T)$ is the anisotropy energy of the system at a particular temperature T . At a temperature slightly below T_C the FM spin-spin correlations become stronger. Further, $M_S(T)$ is almost constant below the transition temperature and hence the decrease in $\chi'(T)$ might be associated with a simultaneous increase in $K(T)$. However, it may also be possible that the observed sharp peak could be the result of both presence of ASD's and local magnetic frustration due to competing interactions between Co-O-Mn for FM and AFM in ECMO.

More interestingly, by comparing out of phase component of AC susceptibility without DC biased and with DC biased at a constant frequency and AC field, we can see an important difference. Firstly, the smaller peaks do not appear under the application of even small DC field which again supports the existence of Griffith like phase. Second, in favor of a typical spin-glass, the peak gets suppressed and peak temperature (T_P) is shifted towards lower temperature with an application of the DC magnetic field. Moreover, we have fitted $T_P(K)$ for different DC fields which follows the de Almeida-Thouless (AT) line,

$$T_P(H) = T_P(0)(1 - AH^{2/3}) \quad (3.1)$$

Where A is constant, $T_P(0)$ and $T_P(H)$ is the value of T_P in the absence of DC bias and with DC bias, and thus it supports the existence of the volume spin-glass-like behavior [172–174]. This is also consistent with what is expected for mean-field scenario [122]. Further, inset of Fig. 3.6(a & c) shows the thermal variation of AC susceptibility, at a fixed AC field = 30e and DC field = 750 Oe with different AC frequencies. Fig. 3.6(e) shows that the peak of the in-phase component of AC susceptibility which is at lower temperature side gets incite and slightly shifts towards lower temperature at a lower frequency. As spins can follow even small

frequency, therefore, these peaks might be due to a slow spin relaxation. In contrast, the origin of the higher temperature side peak is something different, which is expected for long-range ordering and might be due to magnetic transition.

3.3.4 Raman study

Fig. 3.7(a) shows the Raman spectra of ECMO. It consists of many weak Raman bands from that of only two are detectable, one weak band positioned around $\omega_1 \sim 483 \text{ cm}^{-1}$ and another around $\omega_2 \sim 624 \text{ cm}^{-1}$. Band around $\sim 483 \text{ cm}^{-1}$ corresponds to anti-stretching and that of around $\sim 624 \text{ cm}^{-1}$ corresponds to stretching vibrations of the transition metal (Co/Mn) ions

+

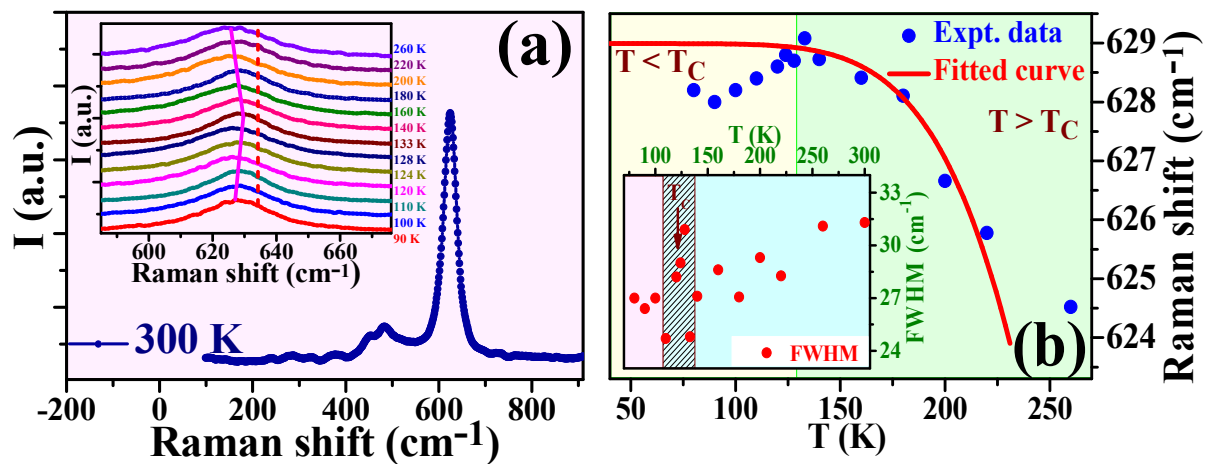


Figure 3.7: (a) Raman spectrum at 300 K and inset consists of Raman spectra taken at different temperature down to 90 K (b) Variation of position of Raman band and FWHM with temperature corresponding to stretching vibrations.

octahedra [37,175–177]. All bands get shifted towards higher wave number side on decreasing temperature down to 128 K [inset of Fig. 3.7(a)]. These shifting follows anharmonic behaviour (shown in Fig. 7(b) as fitted curve) given by the equation [177,178],

$$\omega_{anh}(T) = \omega_0 - C [1 + 2/\{\exp(\hbar\omega_0/k_B T) - 1\}] \quad (3.2)$$

More interestingly, below 128 K bands get slightly shifted towards lower wave number side giving rise to deviation of experimental data points from ideal an-harmonic behaviour. Interestingly this deviation in anharmonicity occurs around magnetic transition temperature (T_C). Further we have observed an anomaly in linewidth i.e., FWHM, shown in the inset of Fig. 3.7(b), around T_C in consistent with earlier report [179]. These are related to a well-known spin-phonon coupling [37,175–179].

3.4 Conclusion

The XPS, UPS, UV-Visible spectroscopy and magnetic properties of ECMO have been investigated. It is observed that Co and Mn are in mixed valence states and ECMO is electrically semiconducting at the room temperature. The observed magnetic transition around 124.5 K is due to the paramagnetic to ferromagnetic/E*-type anti-ferromagnetic phase transition. A clear low-temperature compensation point followed by negative magnetization suggests the existence of anti-phase boundary. Magnetic properties study also indicates the existence of Griffith like phase. Observed MMT has been attributed to the martensitic like phase transition. AC susceptibility measurement suggests the existence of Hopkinson effect, the origin of which might be due to the competing spin-spin correlations and large anisotropy field. Moreover, out of phase component of AC susceptibility with DC biased showed a shifting of peak temperature suggesting the existence of the spin-glass-like behavior under mean-field scenarios. Furthermore, this material also shows a spin-phonon coupling which is clear from the temperature dependent Raman shift. The existence of MMT along with spin-phonon coupling clearly indicates that the system is very important for potential application.

